

Aeroacoustics of an axial ducted low Mach-number stage: numerical and experimental investigation

Miguel Pestana^{1,2,*}; Antonio Pereira^{1,†}; Edouard Salze^{1,‡}; Johan Thisse^{1,2,†}; Marlène Sanjosé^{3,‡};
Emmanuel Jondeau^{1,‡}; Pascal Souchotte^{1,‡}; Michel Roger^{1,§}; Stéphane Moreau^{1,3,§};
Josselin Regnard^{2,‡} and Mathieu Gruber^{2,‡}

¹*Laboratoire de Mécanique des Fluides et d'Acoustique
École Centrale de Lyon & UMR CNRS 5509, 69134 Écully Cedex, France*

²*Département Aérodynamique et Aéroacoustique
Safran Aircraft Engines, 77550 Moissy Cramayel, France*

³*Université de Sherbrooke
Sherbrooke, J1K2R1, QC, Canada*

This paper presents an experimental and numerical investigation of a ducted low-speed axial fan. The stator row is heterogeneous with 3 thickened vanes expected to have a non-negligible impact on the radiated noise. A good agreement for pressure ratio / mass flow rate characteristics is obtained between numerical and experimental results up to the onset of rotating stall. Hot-wire velocity profiles at the inlet assessed the effectiveness of a turbulence control screen added to prevent from inflow distortions. Induct acoustic measurements allowed a detailed description from wall-pressure spectra up to modal decompositions upstream and downstream of the fan. Acoustic modes were identified at the first two blade passing frequencies, which should be cut-off with a homogeneous stator row.

I. Introduction

Ultra High Bypass Ratio (UHBR) engines have the potential for significant reductions in fuel consumption, noise and emissions. However, this kind of architecture requires compact designs and a reduction of the nacelle size. In particular, shorter fan-OGV distances are expected in the near future. A solution is to hold the nacelle by the stator row. Structural elements will then be included in the stator vanes, leading to geometrical and aerodynamic heterogeneities. Those new features will strongly modify the noise generation mechanisms. First, the rotor-stator interaction will be stronger because of the shorter separation. Secondly, the heterogeneity may cause the propagation of modes other than Tyler & Sofrin modes.¹⁻³

This research focuses on several noise mechanisms in a single stage configuration at several flow conditions. The configuration is a low-Mach number ducted axial fan, with several features of future modern fan-OGV architectures. Its tip Mach number at full power is around 0.3, not far from approach conditions of actual turbofans (around Mach 0.5). Three stator vanes of the stage configuration are thicker than the others. This heterogeneity is expected to regenerate propagating modes that would not be excited in a homogeneous

*PhD candidate

†Post-doctoral fellow

‡Engineer

§Professor

configuration. Moreover, the hub to tip ratio and Helmholtz number based on the outer radius allows a significant modal content as in actual turbofans. From a numerical point of view, it allows the comparison of several approaches including Lattice-Boltzmann methods (LBM).

In this paper, the stage configuration is studied using two complementary approaches. First, an experimental campaign is carried out at Ecole Centrale de Lyon, conducted in the *LP3* facility. Aerodynamic measurements are reported to highlight the Turbulent Control Screen (TCS) effects on the inlet flow distortion. The modal content in the duct is deduced from wall-pressure measurements using an inverse method.⁴ Secondly, part of the experimental facility is numerically simulated using steady Reynolds-Averaged Navier-Stokes (RANS) simulations. In the framework of this paper, the numerical approach is only used in order to provide a description of the flow topology.

The paper is organised as follows. The investigated configuration is presented in section II. A first aerodynamic investigation is carried out numerically and experimentally and presented in section III. Then, a chosen operating point is investigated acoustically by means of measurements and presented in section IV.

II. Experimental and numerical strategy

II.A. The *LP3* facility at Ecole Centrale de Lyon

The experiments were conducted in the *LP3* facility in the Centre Acoustique, Ecole Centrale de Lyon in France. The *LP3* facility is an axial low-speed ducted fan, designed and manufactured by Technofan, a subsidiary company of Safran Electrical & Power. The duct is instrumented with both acoustic and aerodynamic sensors.

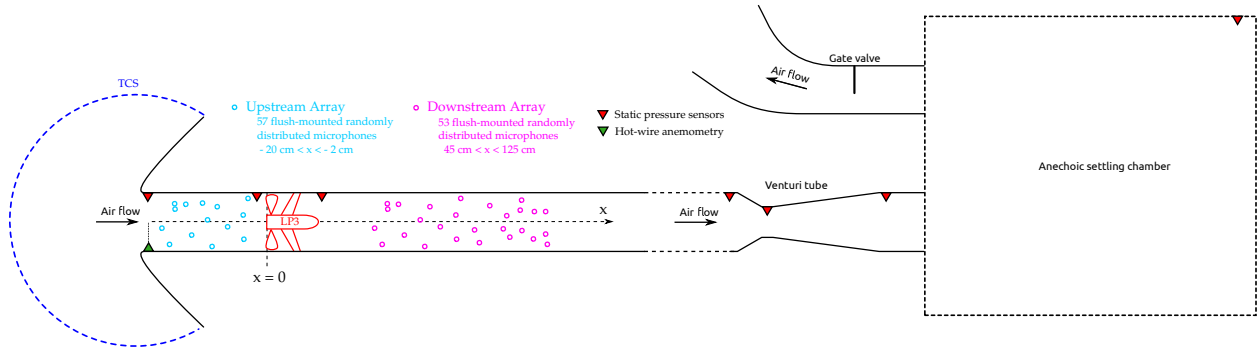


Figure 1. Sketch of the experimental setup.

A sketch of the *LP3* facility is shown in Fig. 1. The fan is configured with $B = 17$ rotor blades and $V = 23$ stator vanes, three of which are thicker for structural purposes, see Fig. 2. The chords of the rotor blades and stator vanes are respectively equal to $C_B = 2.1$ cm and $C_V = 3$ cm. The distance between the rotor blades and the stator row varies from about $0.55C_V$ at the hub to $0.8C_V$ at the tip. The reduced rotor-stator distance emphasizes the blade response to the downstream perturbations (interaction with the potential field generated in the upstream vicinity of the stator vanes). Note that the gap between the blade tip and the casing is large enough to have a strong impact on the noise generation mechanisms too.

Considering a hypothetical homogeneous configuration where all stator vanes would be identical, the first and second blade passing frequencies should be cut-off by the duct. In fact, Tyler & Sofrin's criterion⁵ would predict azimuthal mode orders which are high enough in order to be cut-off at the first two BPFs. However, they are both observed in the duct wall-pressure and far-field spectra. The question whether this is caused by an inflow distortion or by the heterogeneity of the stator motivated the recent installation of a turbulence control screen (TCS), visible in Fig. 3 (right).

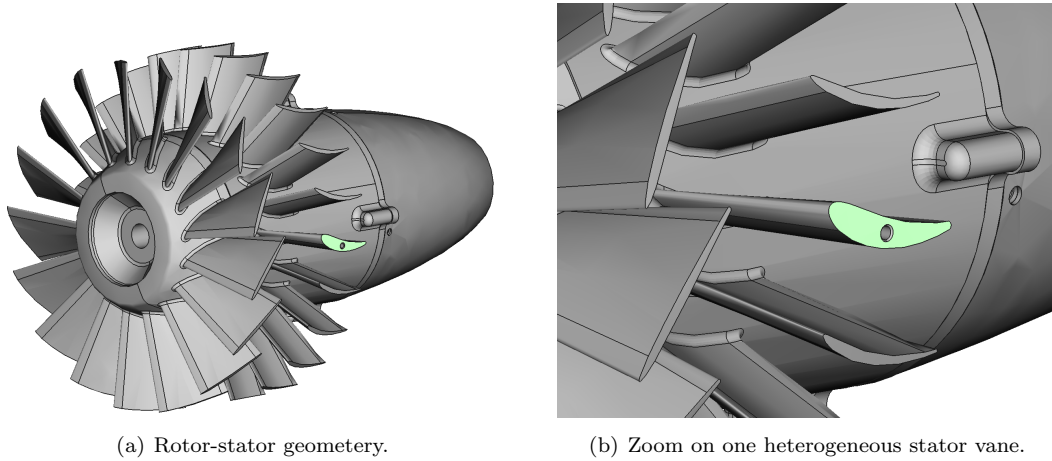


Figure 2. Technofan *LP3* geometry.

The purpose of the TCS is to reduce free stream turbulence, to straighten the flow direction and to remove distortions at the fan inlet. The radius of the TCS is 0.5 m. It covers a portion of three quarters of a sphere centred on the duct inlet. It is made of tens of 2-cm thick plane facets of aluminum honeycomb, stuck together to approach a sphere.

The rotational speed can be adjusted from 2000 rpm to 10000 rpm, the nominal rotational speed. The fan speed is controlled by a PWM controller. A Brüel & Kjær type 2981 laser tachometer is however used to precisely monitor the rotational speed during the experiments (not shown in Fig. 1). The tachometer is placed outside the TCS, the laser beam going through one cell of the honeycomb, so that the inflow conditions are not altered. It produces a voltage pulse for each revolution of the rotor.

Two meters downstream from the stator vanes, a Venturi tube is used to measure the mass flow rate. Downstream from the Venturi tube, air passes inside a $1.5 \times 1.5 \times 2 \text{ m}^3$ anechoic settling chamber. A gate valve is then reached downstream of the chamber. This valve can be gradually closed to fix the operating point of the fan.



Figure 3. Left : Inlet (without the TCS) and instrumented duct. Right : Turbulence Control Screen (TCS). The fan can be seen through the honeycomb.

In the present experiment, two in-duct microphone antennas are used. The first antenna, located upstream of the fan is 20 cm long and made of 57 microphones. The downstream antenna is 80 cm long and made of 53 microphones. Both are equipped with 1/4" Brüel & Kjær type 4957/8 microphones (see Table 1),

flush-mounted behind pinholes. These antennas have been designed and exploited in a previous study, in the framework of the SEMAFOR project.^{4,6} Every single sensor has been calibrated in frequency (amplitude and phase) using a calibration tube and a reference sensor.⁷ Moreover, a global calibration method developed by Leclère *et al.*⁸ has also been applied with success. The calibration results are presented in the section IV.A. Pressure signals are recorded using 18 Brüel & Kjær type 3050 Lan-XI modules. The signals are simultaneously sampled over the 106 microphones at a frequency of 65.6 kHz. In the experiment, the 106 microphones are used to identify the duct-mode amplitudes. The method is described in detail in section IV.C, following previous studies by some of the present authors.^{4,6}

The *LP3* facility is instrumented with 6 static pressure probes at different locations (see Fig. 1). The mean static pressure has been measured with Validyne DP15 transducers and Druck Unik5000 transducers. These measurements have allowed the determination of the pressure rise caused by the fan, and the determination of the mass flow rate at the Venturi tube. Hot-wire anemometry has also been performed at the inlet (see Fig. 1). A Streamline anemometer combined with a Dantec 55P01 hot-wire operating in constant voltage mode provides the streamwise velocity, together with the velocity fluctuations. Geometrical and operating parameters of the *LP3* are summarized in Table 1.

Technofan LP3			Acoustic parameters		
Rotor blades number	B	17	Record time	T	5 min (/OP)
Stator vanes number	V	23	Sampling frequency	F_e	65536 Hz
Heterogeneous stator vanes	V_m	3	Microphone		B&K 1/4-inch
Diameter	\varnothing	17 cm			Type 4957/58
Maximum rotational speed	Ω_{\max}	10000 rpm	Upstream array	N_{mic}	57
Tip Mach number	M_{tip}	~ 0.3		L	20 cm
Max. mass flow rate	Q_m	$\sim 1 \text{ kg}\cdot\text{s}^{-1}$	Downstream array	N_{mic}	53
Max. mean axial flow velocity	U_0	$\sim 40 \text{ m}\cdot\text{s}^{-1}$		L	80 cm

Table 1. *LP3* parameters summary table

II.B. Numerical simulation strategy

In order to accurately investigate the noise generation mechanisms, part of the *LP3* facility is numerically simulated. The numerical domain extends from one radius upstream of the fan to three radii downstream. The numbers of blades B and vanes V of the *LP3* configuration are prime numbers and do not allow a reduction of the simulated domain. For that reason the numbers of blades and vanes are artificially increased to $B = 18$ and $V = 24$. Thus, only a sixth of the domain is simulated. Since the thickness of three stator vanes is different and because those three vanes are not evenly angularly spaced, a full numerical simulation would be required to take into account the true heterogeneity. Again, in order to reduce the grid size, the stator row is assumed to be homogeneous in this simulation. Fig. 10 represents a view of the simplified configuration.

The RANS simulation has been performed with ANSYS CFX V15.0 software using the standard $k - \omega$ SST⁹ turbulent model and a second order spatial scheme. The boundary conditions involve a no-slip condition at the walls, a specified mass flow rate at the inlet and a constant pressure at the outlet. Lastly, a mixing plane is used at the interface between the rotor and the stator.

The mesh consists of 27 millions cells, the boundary layer is fully resolved as the grid resolution is $y^+ = 2$ at the wall. Fig. 5 depicts two grid slices in a meridional plane and in a blade-to-blade plane respectively. The nominal rotational speed is 10000 rpm and the operating point, chosen from the experimental campaign (red square in Fig. 6), is $Q_m = 0.78 \text{ kg}\cdot\text{s}^{-1}$ and $\Delta P = 2100 \text{ Pa}$. Moreover, several mass flow rates were simulated in order to obtain a numerical pressure ratio / mass flow rate performance curve at the nominal

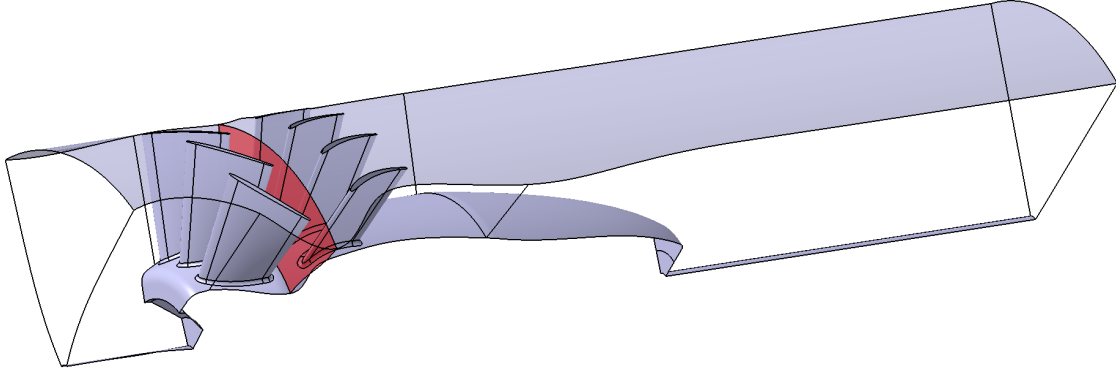


Figure 4. Simplified numerical domain with 3 rotor blades and 4 homogeneous stator vanes. The mixing plane is shown in red.

rotational speed which is plotted with blue squares in Fig. 6.

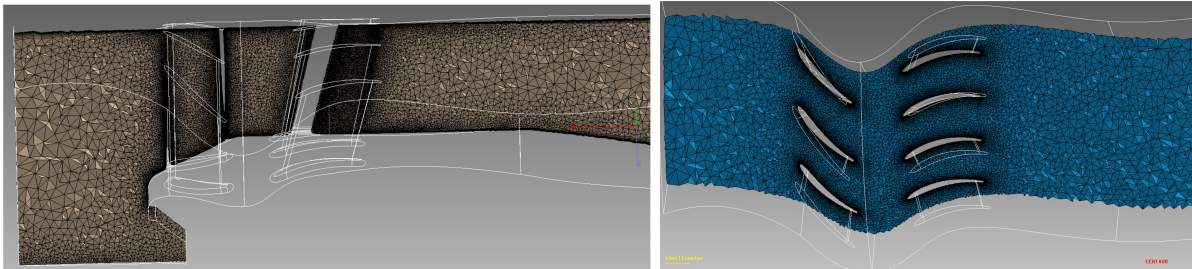


Figure 5. RANS grid; azimuthal (left) and radial (right) views.

III. Aerodynamic investigation

III.A. Operating conditions

Measured pressure ratio / mass flow rate maps¹⁰ are shown in Fig. 6 at 9000 rpm and 10000 rpm respectively. These maps have been obtained with the TCS. When the gate valve is completely open, a maximum mass flow rate of $\sim 1 \text{ kg}\cdot\text{s}^{-1}$ is obtained, at the minimum pressure rise of 1285 Pa. As the gate valve is gradually closed, the mass flow rate decreases and the pressure ratio increases until it reaches a maximum of 2330 Pa (see Fig. 6). Beyond this point, if the gate valve is gradually closed, the fan system exhibits rotating stall and the fan pressure ratio drops dramatically as shown in Fig. 6. No evidence of surge could be observed during the experiments. Returning to normal operating conditions follows a different path, yielding a hysteresis cycle. An example of this hysteresis cycle is plotted at 9000 rpm in Fig. 6 (see gray circles).

Focusing on the numerical simulation, the pressure ratio / mass flow rate characteristic is well reproduced as shown in Fig. 6. The increase in pressure ratio is well captured by the numerical simulation as the mass flow rate is decreased. Moreover, after reaching the maximum pressure ratio, a drop is observed as in experiments for mass flow rates below $0.6 \text{ kg}\cdot\text{s}^{-1}$. The stall position is however under-predicted by the simulation. It is worth noting that phenomena such as the rotating stall are highly unsteady and therefore RANS simulations are not expected to predict them well. Yet the results suggest the presence of this phenomenon with an important pressure drop related to a massive flow separation on the rotor blades. The operating point where the hot-wire velocity profile was performed is indicated as a red circle in Fig. 6.

In order to avoid noise source mechanisms induced by unwanted aerodynamic excitations as the rotating stall,

acoustic measurements were performed at the nominal operating point far from the maximum pressure ratio. The objective is to isolate the heterogeneity effect on classical rotor-stator interaction noise mechanisms. The two operating points where acoustic measurements were performed (at 9000 rpm and 10000 rpm) are shown in Fig. 6 (right). Each of them was done with and without the Turbulence Control Screen introduced in section II.A. During the 5 min of acquisition, performances were recorded every 30 seconds, therefore allowing both mean value and scattering of the data to be measured. It can be clearly seen that the addition of the turbulence screen considerably reduces the performance scattering. This is attributed to the removal of an inlet flow distortion. In other words, the incoming flow is homogenized by the TCS. In consequence, rotational speed variations are also smaller. A more detailed discussion about rotational speed variations is given in section IV.C.

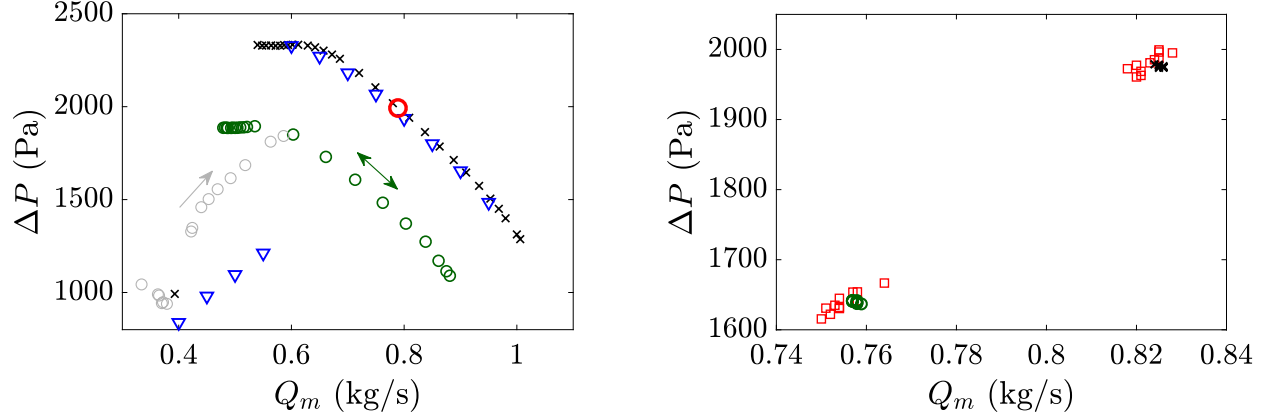


Figure 6. Left : Pressure – mass flow rate characteristics of the *LP3* facility : \times at 10000 rpm and \circ at 9000 rpm. ∇ is the numerical simulation at 10000 rpm. Grey circles \circ indicate the rotating stall cycle recorded at 9000 rpm. The red circle \circ indicates the operating point where a velocity profile has been measured at the inlet using hot-wire anemometry (see Fig. 8 and 9). Right : The two operating points where modal decompositions were performed : \circ at 9000 rpm and \times at 10000 rpm with TCS. Respective results without TCS in \square .

III.B. Hot-wire inlet velocity profiles

It has been reported several times that the inflow conditions of a ducted fan differ from the flight conditions that a realistic engine would encounter.^{11,12} In particular, an isolated ducted fan is subjected to an inflow distortion. This inflow distortion may act as an acoustic source at the blade passing frequencies. The role of the TCS is first to attenuate free-stream turbulence, and also to suppress this inflow distortion in such a way that the fan is fed with an axi-symmetric flow. In previous experimental campaigns at the *LP3* facility, an inflow distortion was evidenced by a smoke generation technique as shown in Fig 7. The streamlines of an inlet vortex can be clearly observed.

To validate the efficiency of the TCS, velocity profiles have been measured in the inlet of the *LP3* facility. Velocity profiles in the x direction are given in Figs. 8 and 9, with and without TCS. Close to the wall ($r/R = 0.98$), both cases exhibit a mean velocity \bar{U} 18% higher than the velocity at the center of the duct U_0 (see Fig. 8). This effect is due to the inlet geometry. At this measurement station, without the TCS, the boundary layer momentum thickness is $\theta = 1.8$ mm, and the shape factor is $H = \delta^*/\theta = 1.18$. Such a shape factor denotes a completely developed turbulent boundary layer. These values are not modified with the TCS.

Contrary to the mean velocity profiles, the fluctuating velocity profiles exhibit considerable differences with and without the TCS. In Fig. 9 (left), the TCS is observed to homogenize fluctuations at a level of 0.5% in the duct center. Without TCS, fluctuations had radial variations up to 1.5%. These results confirm the TCS effectiveness regarding the removal of the inflow distortion and disturbances. Regarding the boundary layer region plotted in Fig. 9 (right) a maximum of about 5% of velocity fluctuations is observed with TCS

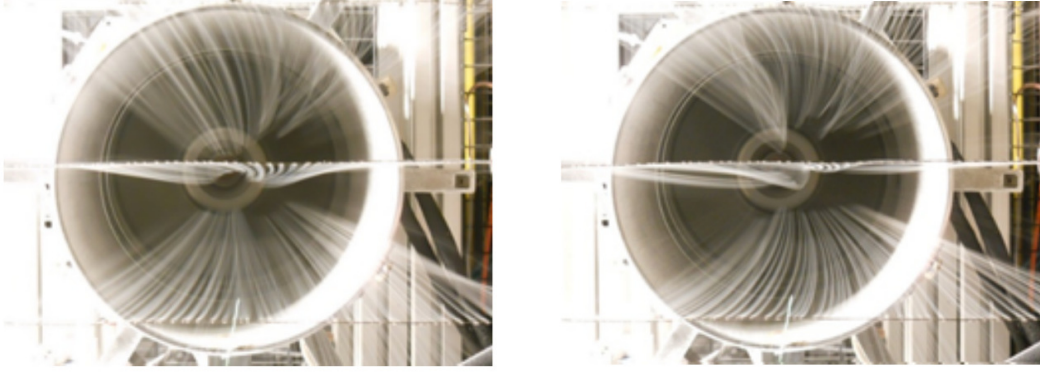


Figure 7. Inflow distortion visualization at the *LP3* facility with a smoke generation technique. Two successive time snapshots. Visualization obtained in the framework of previous investigations by K. Kucukcoskun at the LMFA.

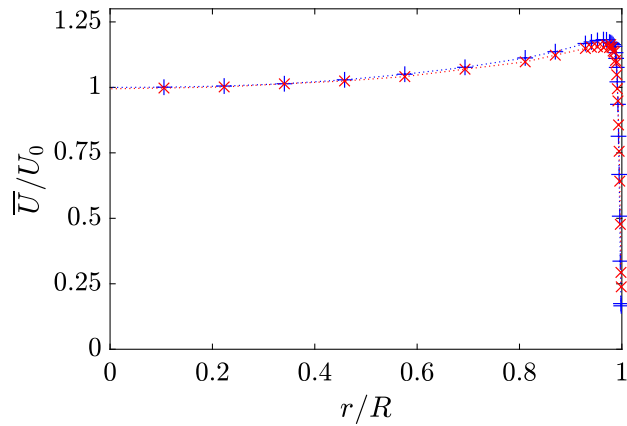


Figure 8. Mean velocity profiles, measured in the inlet using hot-wire anemometry. $U_0 = 28.3 \text{ m.s}^{-1}$ denotes the velocity at the center of the duct, and R denotes the radius of the duct. + : with TCS ; x : without TCS

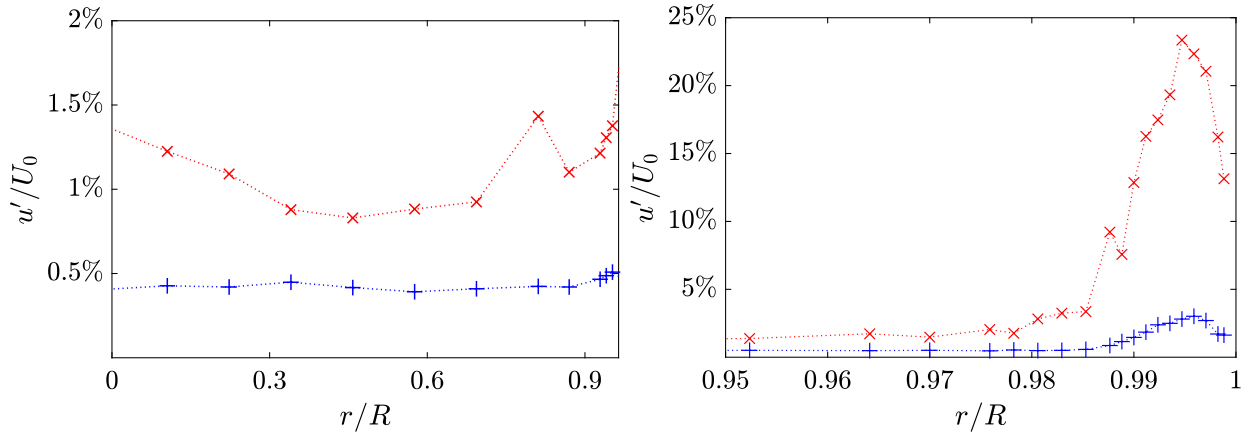


Figure 9. Root-mean squared velocity fluctuations u' profiles, measured in the inlet using hot-wire anemometry. At left : centre region. At right : boundary layer region. $U_0 = 28.3 \text{ m.s}^{-1}$ denotes the velocity at the center of the duct, and R denotes the radius of the duct. + : with TCS ; x : without TCS

at $r/R = 0.995$, which is due to the wall-bounded turbulence. Without the TCS, values up to 27% are observed in the same region. To further investigate this point, examples of velocity signals are plotted in Fig. 10. It can be seen from Fig. 10a that the huge velocity fluctuations observed without TCS originate

from random velocity defects, rather than from turbulence. It is therefore plausible that such high values of velocity fluctuations are caused by vortices randomly ingested by the fan. This inflow distortion is completely corrected when the TCS is used (see Fig. 10(b)). Another advantage is that, with the TCS, the operating point of the fan is completely stabilized, see Fig. 6 (right). In particular, the first point where rotating stall is encountered is located higher in the pressure – mass flow rate characteristics. The TCS therefore allows the fan to be operated at higher pressure ratios, where the fan is supposed to exhibit a higher efficiency.

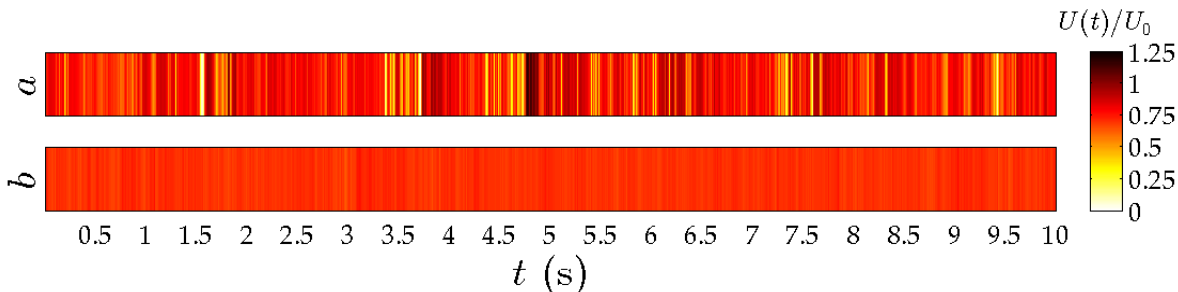


Figure 10. Examples of velocity signals $U(t)$ recorded by hot-wire anemometry at the nominal operating point (see Fig. 6) in the inlet, at $r/R = 0.988$. a) Without TCS ; b) With TCS.

III.C. Steady RANS results

In this section, aerodynamic results from the numerical simulation are investigated. The Mach number and the entropy fields are plotted in Fig. 11 at two spanwise locations. An important flow separation occurs at the vane tip (Fig. 4, bottom). Because of the mixing plane, the flow coming from the rotor is azimuthally averaged and no unsteady wake interaction between the rotor blades and the stator vanes can be captured.

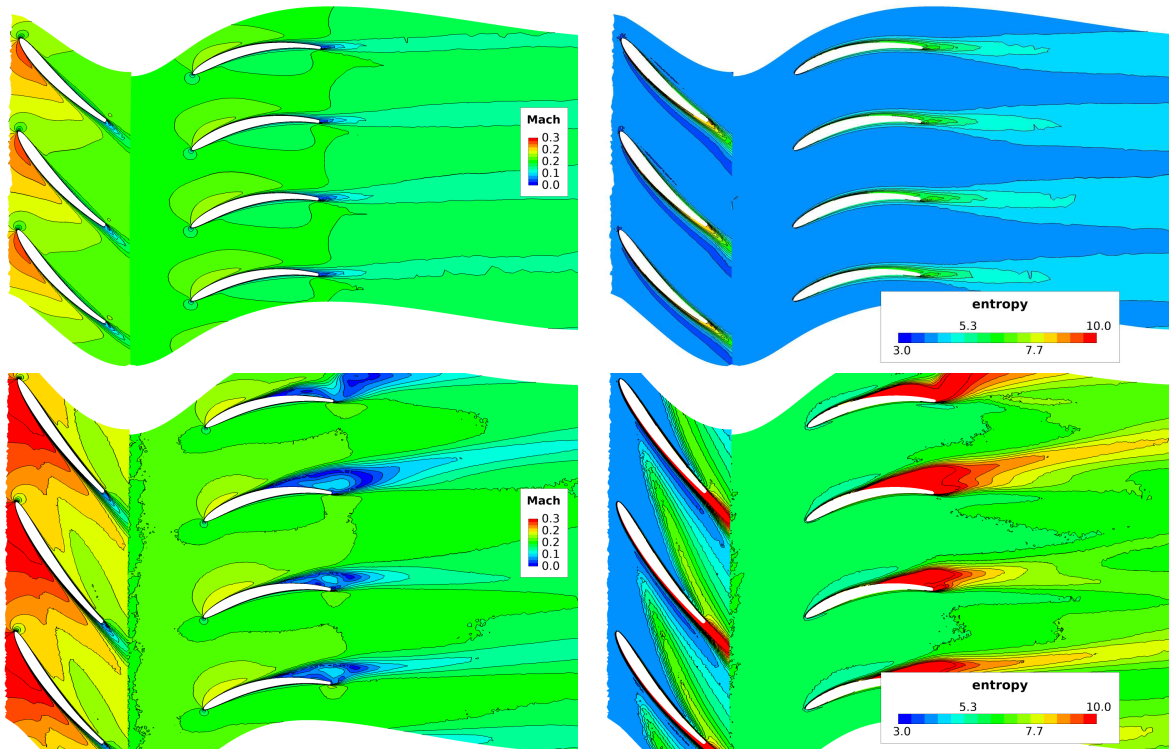


Figure 11. RANS calculation; Mach number (left) and entropy (right) at 52.5% (top) and 95% (bottom) of the span.

Fig. 12 represents the static pressure and the friction lines of one rotor blade and one stator vane. Contrary to the rotor, a flow separation occurs at the vane suction side (see Fig. 12, bottom, right). This kind of corner separation was investigated by Zambonini and Ottavy.¹³

Besides the classical rotor-stator interaction noise mechanisms, one can expect important sources resulting from the unsteadiness associated to the observed corner vortices on the stator vanes.

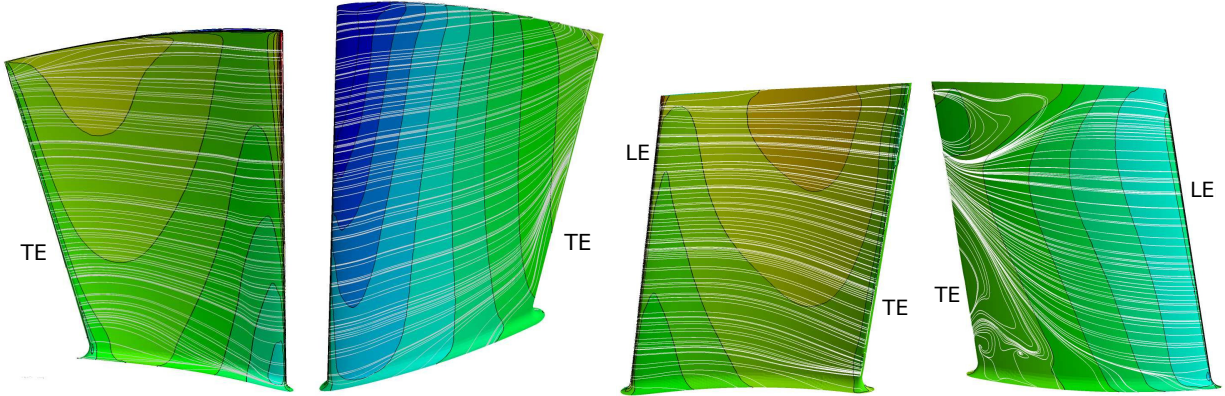


Figure 12. Rotor blades (left) and stator vanes (right) colored by the static pressure and friction lines.

IV. Acoustic investigation

This section is devoted to the acoustic investigation of the *LP3* facility. All measurements are performed via in-duct flush-mounted microphone arrays placed upstream and downstream of the fan module, see Figs. 1 and 3. First, the microphone calibration procedure is detailed in section IV.A. Wall-pressure spectra are then shown in section IV.B. Next, modal decomposition of the acoustic pressure field is done from the microphone array data. This is done in order to assess the modal content of the noise generated by the *LP3* fan. Results are presented in section IV.C. Finally, section IV.D presents an investigation on the influence of cut-off modes which must be taken into account in certain conditions.

IV.A. Microphone calibration

In the framework of this study, microphones are mounted behind a pinhole cap as shown in Fig. 13. This mounting was chosen because the protection grid microphones is not removable. It can be seen that a small cavity between the microphone membrane and the pinhole is created and this will be at the origin of acoustic resonances at discrete frequencies. For this reason, a calibration process is essential in order to retrieve a correcting transfer function for each microphone. It will relate the actual pressure measured by the microphone to the pressure of interest at the duct wall.

To perform the microphone calibration, two methods have been compared: an individual *local* method and a global *non-local* one.

The individual method must be performed for each microphone using a calibration device described in.^{7,8} A loudspeaker (driver unit) is used to generate a broadband signal (white noise) covering the frequency band of interest. The source is deported using a hose at the end of which the calibration device is located. In the calibrator, a 1/4 inch microphone is used as a reference microphone. The calibrator is then placed against the surface on which the pinhole is mounted. Once the calibration device is in place and the noise generator active, signals from both the reference microphone and the pinhole-mounted microphone are recorded simultaneously. It has been checked that the coherence was very close to unity over a wide frequency band and up to the cut-off frequency of the calibration duct device. From these two signals, the transfer function between both microphones can be finally obtained. In other words, the frequency response

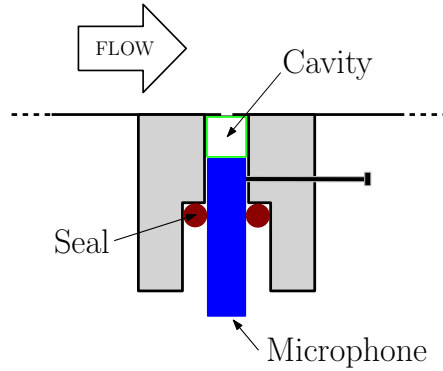


Figure 13. Microphone slot scheme.

of the pinhole is measured. This method of calibration nevertheless has some disadvantages. One of them is related to the repeatability of the calibration procedure, which is very sensitive to the calibrator position in front of the pinhole. Secondly, once the array is installed, some microphones are inaccessible such that the calibration device cannot be correctly placed.

For this reason, a second method, hereafter called global, has been used. This method consists in placing the artificial source (i.e. driver unit) at one termination of the duct and to record the signals from all microphones at once. An axial duct section is added between the source and the array to ensure that only cut-on modes are measured by all microphones. Finally, the application of the method developed by Leclère et al.⁸ leads to the frequency response of the pinhole sensor. The advantage of this approach is that all microphones are calibrated at once and it can be done even in the presence of obstacles (see the fan module) in between the artificial source and the array. Although, it should be noted that the distance between the obstacle and the array has to be large enough in order to capture only cut-on modes.

Comparisons between the two methods for one microphone of the downstream array are given in Fig. 14. Resonances at around 1 and 3 kHz caused by the cavities can be observed. The individual method (in black) shows a divergence behaviour at ~ 12 kHz. In fact at those frequencies the wavelength becomes of the same order of magnitude as the distance between the reference microphone placed in the calibrator and the pinhole. This is indeed the frequency limitation of this method. The global method (in red) is also able to recover the frequency response with an excellent agreement. Again, at high frequencies the method reaches a limitation due to the increased number of cut-on modes. In that case, regularization methods are used in order to improve the matrix inversion problem. In particular, the resolution of the system of equations is here under-determined, as the number of modes is higher than the number of available microphones. Globally, this method offers a better repeatability compared to the individual method. The global calibration method is therefore used in the present study.

IV.B. Wall-pressure spectra

In Fig. 15, the averaged spectra of all microphones are presented for the upstream and downstream array. Acoustic pressure signals have been averaged over the 5 min of acquisition using a fixed time window of 1 s duration, an overlap of 60% with a Hanning window.

In those spectra, broadband and tonal components can be seen. It is important to note that, at this stage, the hydrodynamic part of the wall-pressure has not been removed. Thus, the broadband component observed is mainly dominated by the boundary layer pressure fluctuations associated with turbulence. Even though, the acoustical part is also contained and related to the boundary layer associated noise, trailing edge noise and turbulence impingement noise. Levels are about 20 to 30 dB below the tonal noise and are higher by up to 15 dB at low frequencies for the downstream array.

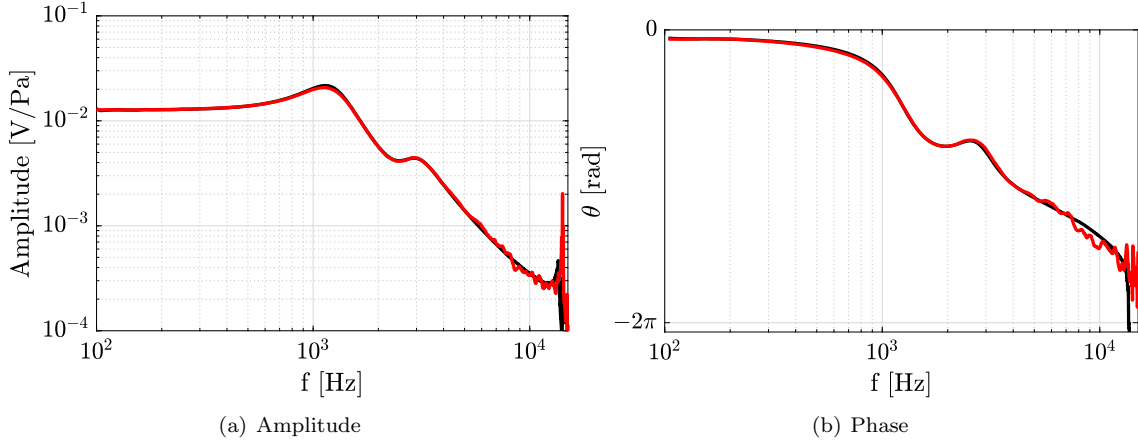


Figure 14. Frequency response comparison between individual method — and global method — of the microphone N°14 for the downstream array.

On the other hand, the tonal noise component is caused by interactions occurring at the blade passing frequencies. In Fig. 15, only the first three BPF are plotted. This component is mainly caused by the rotor-wake impingement on the stator vanes as well as the rotor interaction with the potential field generated upstream of the stator. As previously mentioned, the first two BPFs should be cut-off considering the number of blades and vanes of the *LP3*. They are seen to be highly effective with levels higher or comparable to the third BPF depending on the array. The addition of the turbulence control screen is observed not to remove the BPFs but to sharpen them. It is an expected result accounting for the inlet distortion removal described in section III. In fact, the presence of an unsteady distortion moving in time at the fan inlet (see Fig. 7) will cause the broadening of the BPFs as observed for results without TCS. At this point, the heterogeneity of the stator remains the only track of explanation for the radiating noise at the first two blade passing frequencies.

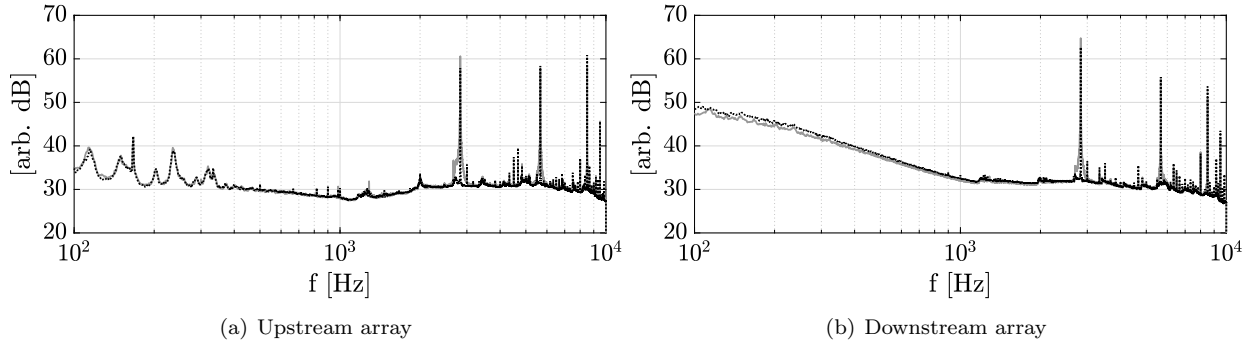


Figure 15. Mean spectra of all microphones of the upstream and downstream array. --- with TCS and — without TCS. $Q_m = 0.82 \text{ kg}\cdot\text{s}^{-1}$ and $\Delta P = 1980 \text{ Pa}$. Frequency resolution of 1 Hz.

For a more detailed analysis around the blade passing frequencies, the wall-pressure fluctuations measured by a single microphone have been analyzed. Results have been compared with and without TCS. The microphone belongs to antenna # 1 (see Fig. 1), located about 30 mm upstream of the rotor. The broadband contribution is unchanged by the TCS, but the tonal components at the blade passing frequencies are different (see Fig. 16). With TCS, at the blade passing frequencies, the spectra exhibit a pure tone. Without the TCS, the peak is widened, which is typical of an unstable wandering inlet vortex.^{11,14} In addition, the level of the peak is diminished with the TCS. Depending on the microphone location, reductions of up to 10 dB can occur (see Fig. 16).

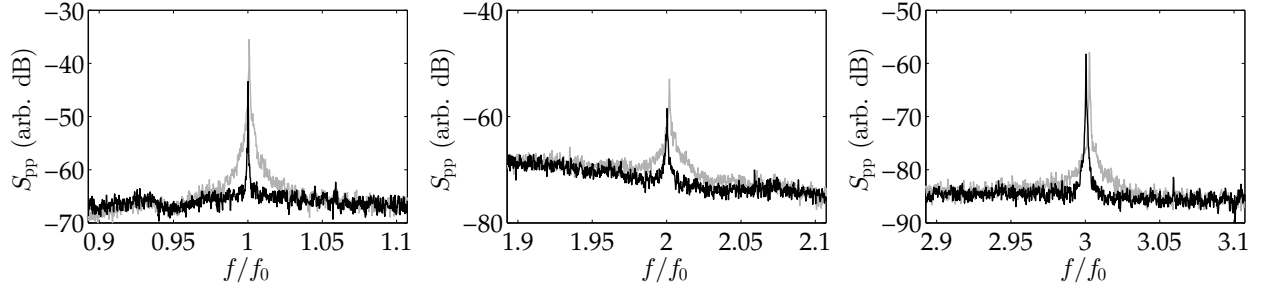


Figure 16. Wall-pressure spectra measured at the inlet, centered around the first (at left), the second (center) and the third (at right) blade passing frequencies, here denoted as f_0 . — : without TCS ; - - : with TCS. Frequency resolution of 1 Hz.

IV.B.1. Accounting for rotational shaft speed variations

It is proposed in this section to account for possible rotational speed variations. For this purpose, the signal of the tachometer described in section II is measured simultaneously with the microphones. In order to give a few orders of magnitude, rotational speed variations for several operating points are summarized in Table 2. The calculation of an equivalent frequency variation is also given. Globally, it can be seen that the coefficient of variation (cv) is always below one percent for all cases considered. Nevertheless, if the associated frequency variation is calculated, variations up to 14 Hz can be obtained without TCS, which constitutes an important variation.

It is observed that the addition of the TCS considerably reduces rotational speed variations. This confirms the previous result observed in the pressure rise ΔP vs Q_m plot shown in Fig. 6 (right). It may be deduced that a homogenized inflow reduces considerably the unsteadiness of the rotational speed.

Q_m [kg.s ⁻¹]	ΔP [Pa]	without TCS		with TCS	
		cv Ω [%]	Δf [Hz]	cv Ω [%]	Δf [Hz]
1.02	1300	0.38	± 11	0.14	± 4
0.82	1980	0.48	± 14	0.12	± 3
0.79	2059	0.39	± 11	0.11	± 3
0.76	2134	0.39	± 11	0.12	± 3
0.62	2359	0.39	± 11	0.11	± 3
0.55	2368	0.45	± 13	0.17	± 5

Table 2. Rotational speed variations and corresponding frequency variations for several operating points at 10000 rpm with and without TCS.

During a second, several complete revolutions of the rotor take place at the considered speeds. Now, if the rotational speed varies, this implies that a different number of revolutions may be contained on successive blocks of one second. To avoid this, the tachometer signal is used to locate when the rotor completes a full revolution. The signal is then interpolated on a grid and time signals are averaged for each revolution. Thus, if the number of averages is large enough, the deterministic part of the signal associated with the rotational speed is isolated. The following analyses are then expressed in engine orders. An engine order has a direct relation with the frequency as expressed in Eq. 1.

$$f_{\text{BPF}} = \frac{sB\Omega}{60} \quad \longrightarrow \quad \text{EO}_{\text{BPF}} = sB \quad (1)$$

It is then possible to recalculate spectra after the averaging procedure. Results are presented in Fig. 17. At all operating points, there is a significant reduction in the broadband level by more than 20 dB. A series of tones are revealed with the reduction of the broadband level. These tones were investigated and are

harmonics of the rotational shaft frequency. The origin of those tones remains unexplained but could be linked to inhomogeneities in the rotor geometry or in the rotor-blade wakes. Further investigations with rotor-wake measurements should allow a better understanding of those tones. Nevertheless, the level of BPF remains almost unchanged indicating a weak effect of the speed variations on tonal noise.

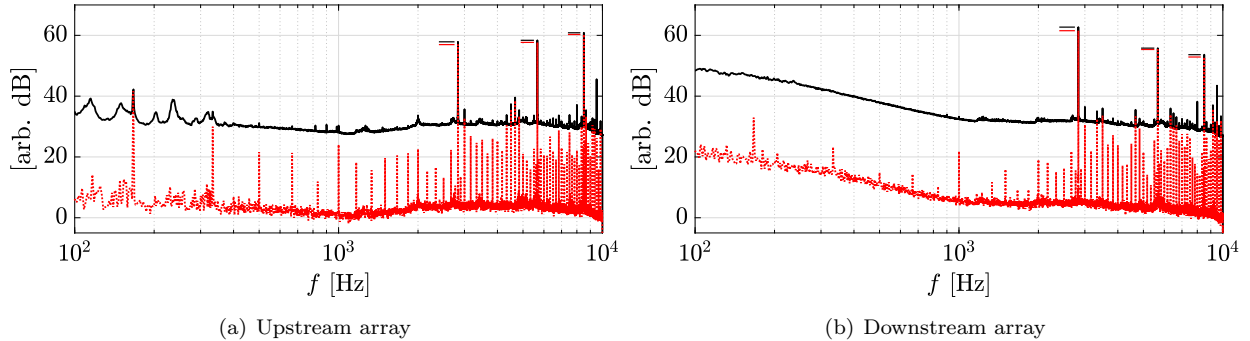


Figure 17. Mean spectra of all microphones of the upstream and downstream array. — is the time-average spectrum and — the rotor-locked averaged spectrum. $Q_m = 0.82 \text{ kg}\cdot\text{s}^{-1}$ and $\Delta P = 1980 \text{ Pa}$. Frequency resolution of 1 Hz.

Finally, a further analysis is given on the broadband noise component by investigating the cross-spectrum (in blue) of two close microphones of the downstream array plotted in Fig. 18. Both microphones have the same axial position and are angularly separated by 25 degrees ($\sim 40 \text{ mm}$). The auto-spectrum (in black) and the rotor-locked averaged spectrum (in red) of the first microphone are also added. One can see that levels of the cross-spectrum can be 10 dB below the auto-spectrum. In fact, as mentioned before, since the turbulence correlation length is smaller than the distance between the two microphones, off-diagonal terms of the cross-spectral matrix are partly depolluted from turbulent fluctuations. At low frequencies, where the correlation length becomes comparable to the microphone separation distance, levels of both auto- and cross-spectrum merge. Finally, the rotor-locked spectrum presents even lower levels because all the non-deterministic part of the pressure signal is greatly removed by the averaging procedure.

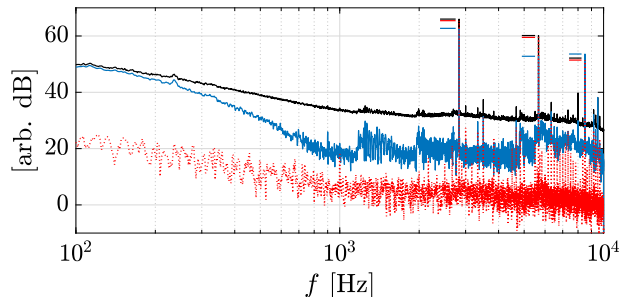


Figure 18. Spectra of two closely spaced microphones. In — is the auto-spectrum of the first microphone, in — the cross-spectrum of the two microphones and in — the rotor locked spectrum of the first microphone. $Q_m = 0.82 \text{ kg}\cdot\text{s}^{-1}$ and $\Delta P = 1980 \text{ Pa}$. Frequency resolution of 1 Hz.

IV.C. Modal decomposition

In this section, modal decompositions are performed using the measured pressure fluctuations acquired by each array. The objective of this modal decomposition is to assess the modal content of the fan module and to investigate which modes are predominant.^{15–22} It is expected that modes related to the stator heterogeneity at the first two BPFs (cut-off in a homogeneous configuration) will be highlighted. Considering a hard-walled duct of circular cross-section, the acoustic pressure at any point inside the duct can be expressed as a sum of modes as follows^{23,24}

$$p(x, r, \theta, t) = \sum_{m=-\infty}^{+\infty} \sum_{n=0}^{+\infty} \frac{f_{mn}(r)}{\Gamma_{mn}} \left[A_{mn}^+ e^{i\gamma_{mn}^+ x} + A_{mn}^- e^{i\gamma_{mn}^- x} \right] e^{im\theta} e^{-i\omega t}, \quad (2)$$

where the pressure p is measured (known), A_{mn}^\pm are the modal amplitudes (unknowns) and f_{mn} the radial shape functions. A detailed description of the modal basis parameters is given in Appendix A. At positions relatively far from sources or duct discontinuities, this infinite sum may be well-approximated by taking only those terms related to cut-on modes. Considering that the array is made of M microphones and assuming that there are N cut-on modes, Eq.(2) may be conveniently expressed in a matrix form as:

$$\mathbf{p} = \mathbf{\Phi} \mathbf{c}. \quad (3)$$

This formulation is better suited for numerical resolutions in which a matrix inversion must be performed. The solution is then given by

$$\hat{\mathbf{c}} = \mathbf{\Phi}^\dagger \mathbf{p}, \quad (4)$$

where the notation \square^\dagger stands for the pseudo-inverse of $\mathbf{\Phi}$. In the framework of our study, an equivalent formulation is used. It introduces the notion of the Cross-Spectral Matrix (CSM) defined as follows

$$\mathbf{S}_{\mathbf{p}\mathbf{p}} = \mathbb{E} \{ \mathbf{p}(\omega) \mathbf{p}(\omega)^H \}, \quad (5)$$

where \square^H is the Hermitian operator and the notation $\mathbb{E} \{ \square \}$ stands for the expected-value operator. In practice, an estimate of $\mathbf{S}_{\mathbf{p}\mathbf{p}}$ is obtained by averaging the outer product $\mathbf{p}(\omega) \mathbf{p}(\omega)^H$ over a finite number of snapshots (time blocks). Eqs. (3) and (4) along with the definition in Eq.(5) yield:

$$\hat{\mathbf{S}}_{\mathbf{c}\mathbf{c}} = \mathbf{\Phi}^\dagger \hat{\mathbf{S}}_{\mathbf{p}\mathbf{p}} \mathbf{\Phi}^{\dagger H}, \quad (6)$$

where the matrix $\hat{\mathbf{S}}_{\mathbf{c}\mathbf{c}}$ is a cross-spectral matrix of modal amplitudes. Diagonals contain auto-spectra of individual modes and off-diagonals terms are cross-spectra between all pairs of modes. In some cases, such as near cut-off frequencies, as well as frequencies at which the number of cut-on modes is large when compared to the number of microphones, the matrix $\mathbf{\Phi}$ may be ill-conditioned. In this case more involved techniques must be used to compute its inverse.⁴

IV.C.1. Broadband noise

A difficulty in the analysis of fan broadband noise using wall flush-mounted probes is the fact that pressure fluctuations are largely dominated by wall-bounded turbulence. As it will be seen in the next section, for the tonal noise component, this problem is minor since the fan-related noise largely emerges from the hydrodynamic component, by at least 20 dB. In contrast, for the broadband component, the signal of interest might be about 10 dB lower. Thus, to perform a modal decomposition of the broadband noise component, an additional treatment is needed to extract the fan-associated noise.

At low Mach numbers, the turbulence length scales are much smaller than the separation distance between two neighboring microphones, contrary to the much higher correlation length of acoustic waves. This implies that the hydrodynamic contribution is mainly contained in the diagonal of the cross-spectral matrix, whereas off-diagonal terms contain information about the sound waves.

To remove this hydrodynamic contribution, different methods are proposed in the literature.^{7,25-27} A common practice consists in removing the cross-spectral matrix diagonal, by setting diagonal entries to zero. Nevertheless, this approach removes the properties of a CSM matrix and can lead to *non-physical* negative modal amplitudes. To avoid this issue, another method is adopted in this study allowing to decompose the CSM into acoustic and hydrodynamic parts, as shown by Finez et al.⁶ In a few words, the idea of the method is to exploit the different structures of the CSM associated with acoustic and hydrodynamic parts to help their separation. The method returns an estimate of the CSM with reconstructed auto- and cross-spectra and thus preserves the property of positive semi-definiteness of a cross-spectral matrix.

Results are plotted in Fig. 19 for the upstream array and in Fig. 20 for the downstream array. They show the modal amplitudes at cut-on azimuthal orders as a function of frequency. As predicted by the duct acoustics theory, the number of cut-on modes increases with frequency. To highlight the level of the broadband contribution, the colormap was saturated at 20 dB. With this, the tonal component of noise appearing at the BPF will often be saturated. In addition, a sum over the radial modes is made to simplify the interpretation.

A slight predominance of co-rotating modes ($m > 0$) can be observed. However, for low-speed fans like the *LP3*, a strong imbalance between co- and counter-rotating modes is not expected to be as dominant as it would be for a turbofan.^{28,29} Secondly, it can be seen that the energy is fairly concentrated near the cut-off region (see Ganz et al.²⁹) with deviations up to 10 dB from the central zone.

The addition of the TCS tends to remove the spectral broadening observed around BPFs. The tonal component is more concentrated at a precise frequency as observed before, confirming the effectiveness of the TCS.

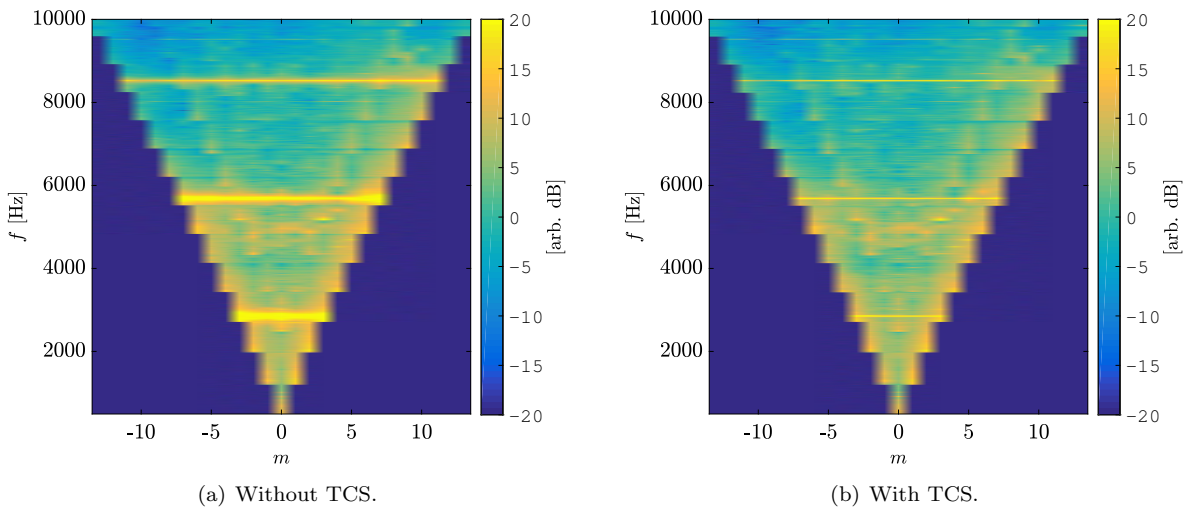


Figure 19. Broadband modal content of the upstream array with and without TCS. $Q_m = 0.82 \text{ kg}\cdot\text{s}^{-1}$ and $\Delta P = 1980 \text{ Pa}$. Frequency resolution of 8 Hz.

Conclusions are similar for both arrays. Nevertheless, the upstream array (plotted in Fig. 19) presents higher levels by around 5 dB in the region between the first and second BPF. The short distance between the fan and the antenna may be at the origin of this increase. In addition, an internal v-shape modal structure related to the radial order $n = 1$ is seen. This is due to the summation over radial orders used in the analysis.

IV.C.2. Tonal noise

In this section, the interest is focused on the tonal noise at the blade passing frequencies. Again, results are presented in terms of azimuthal orders and summed over radial orders. Both the upstream and downstream modal contents of the fan will be compared.

In this frequency analysis, rotational speed variations are not taken into account. Time-averaged modal decompositions are performed. Results for the first, second and third BPFs are presented in Figs. 21 (a-c). As a reminder, within the framework of a perfectly homogeneous fan-OGV geometry, the first two BPFs should be cut-off. That is to say, the rotor/stator interaction modes generated would be of an azimuthal order high enough to be cut-off.

For the first BPF in Fig. 21(a), the mode of order $m = -3$ emerges by about 8 dB from the other modes for both arrays. However, the amplitude on the downstream antenna is nearly 3 dB higher than on the

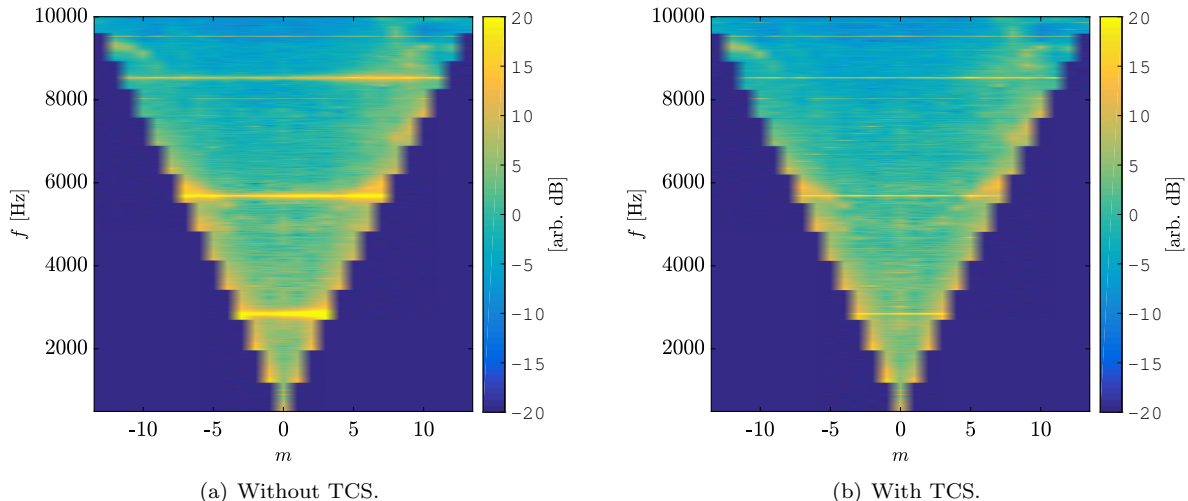


Figure 20. Broadband modal content of the downstream array with and without TCS. $Q_m = 0.82 \text{ kg}\cdot\text{s}^{-1}$ and $\Delta P = 1980 \text{ Pa}$. Frequency resolution of 8 Hz.

upstream antenna. In fact, this can be verified in section IV.B where spectra have been presented (see Fig. 15). In those spectra, the first BPF tone is higher for the downstream array.

The second BPF results are presented in Fig. 21(b). Modes of order $m = 5$ and $m = 7$ for the upstream antenna emerge by 3 and 4 dB. For the downstream array, the mode $m = 7$ is dominant by 3 dB. Contrary to the first BPF, levels are more important for the upstream antenna as observed in spectra presented in section IV.B.

Finally, at the third BPF presented in Fig. 21(c), modes of order $m = 5$ and $m = 11$ prevail by 3 to 7 dB respectively. Again, amplitudes are stronger for the upstream array as previously observed in Fig. 15. The mode $m = 5$ is in fact well predicted by the classical Tyler & Sofrin's criterion as evidenced in Eq. 7. For the third BPF ($s = 3$), the lower mode that can be generated corresponds to $p = 2$ leading to the final order $m = 5$.

$$m = sB - pV = 3 \times 17 - 2 \times 23 = 5 \quad (7)$$

To conclude, some modes were identified to predominate at the first three blade passing frequencies. By considering that the inflow distortion is removed with the addition of the turbulence control screen, those modes are expected to be generated by heterogeneous rotor-stator interaction.

IV.C.3. Accounting for rotational shaft speed variations

To ensure that the modes observed in the previous analysis are related to deterministic interactions related to the rotational speed, we now take into account speed variations. Modal decompositions are then carried out on the basis of the signals resulting from synchronous averaging. Results are shown in Fig. 22 for the first three blade passing frequencies. On those plots, a direct comparison is done with previous results (shown in Fig. 21) for the downstream array.

The results are very close from those obtained with the time-average processing which did not take into account speed variations. A slight attenuation is observed when compared with the previous amplitudes. It indicates that a small part of the energy could have been associated with broadband phenomena or due to speed variations. However, the difference is minimal and modes identified previously are indeed generated by deterministic phenomena associated with the rotational speed. The inflow distortion was shown to be greatly removed by the TCS and tones at multiples of the shaft speed are considerably lower in level than those multiples of the blade passing frequencies. Hence, the identified modes can be expected to be

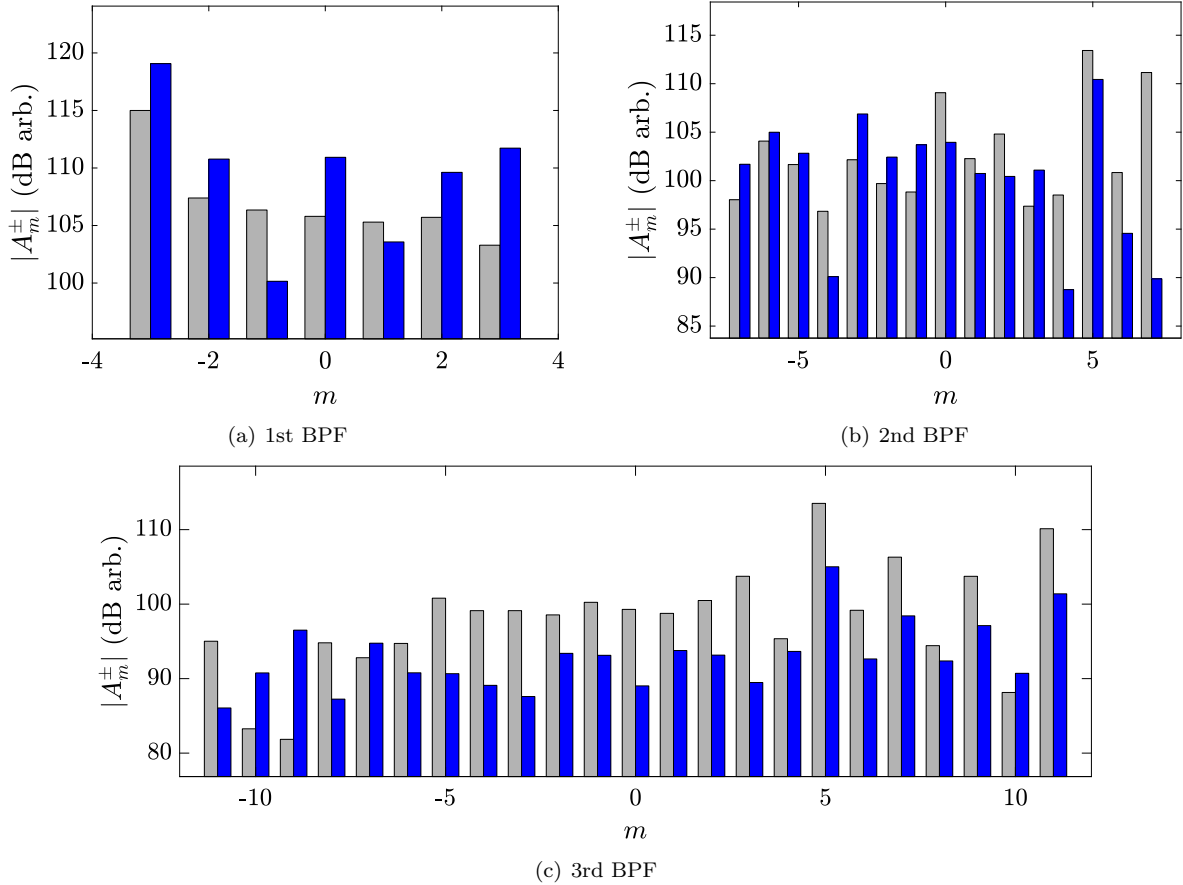


Figure 21. Tonal modal content of the upstream (in grey) and downstream array (in blue) with TCS (frequency analysis). $Q_m = 0.82 \text{ kg}\cdot\text{s}^{-1}$ and $\Delta P = 1980 \text{ Pa}$

generated by rotor-stator interaction and the emergence of tones at 1BPF and 2BPF possibly explained by the heterogeneity of the stator. Future LBM simulations will allow improving the understanding and quantification of the heterogeneity impact on the rotor-stator tonal noise and to check if the identified modes are retrieved.

IV.D. Accounting for cut-off modes

In this last section, the influence of cut-off modes is investigated. The close distance of the antenna upstream from the $LP3$ motivates this study. Indeed, when modal decomposition has been applied for a smaller rotational speed (9000 rpm), the fit between measured and reconstructed data was very low. This indicates that modal amplitudes recovered through modal decomposition hardly explains the measured pressure. One possible reason is the presence of cut-off modes not considered in the model.

It is important to note that a different rotational speed leads to a different number of cut-on modes. As an example, the highest cut-on azimuthal orders are $m \in [-3, 3]$ for 10000 rpm and $m \in [-2, 2]$ for 9000 rpm. It is then important to investigate if the mode $m = 3$ now cut-off at 9000 rpm has a rate of decay sufficiently strong to not contaminate microphones of the upstream antenna.

For this, one can study the axial evolution of modes defined by their axial wave-number defined as follows :

$$k_{mn} = \sqrt{k_0^2 - \beta^2 K_{mn}^2} \quad (8)$$

where k_0 is the acoustic wave-number related to the considered rotational frequency, β is the compressibility

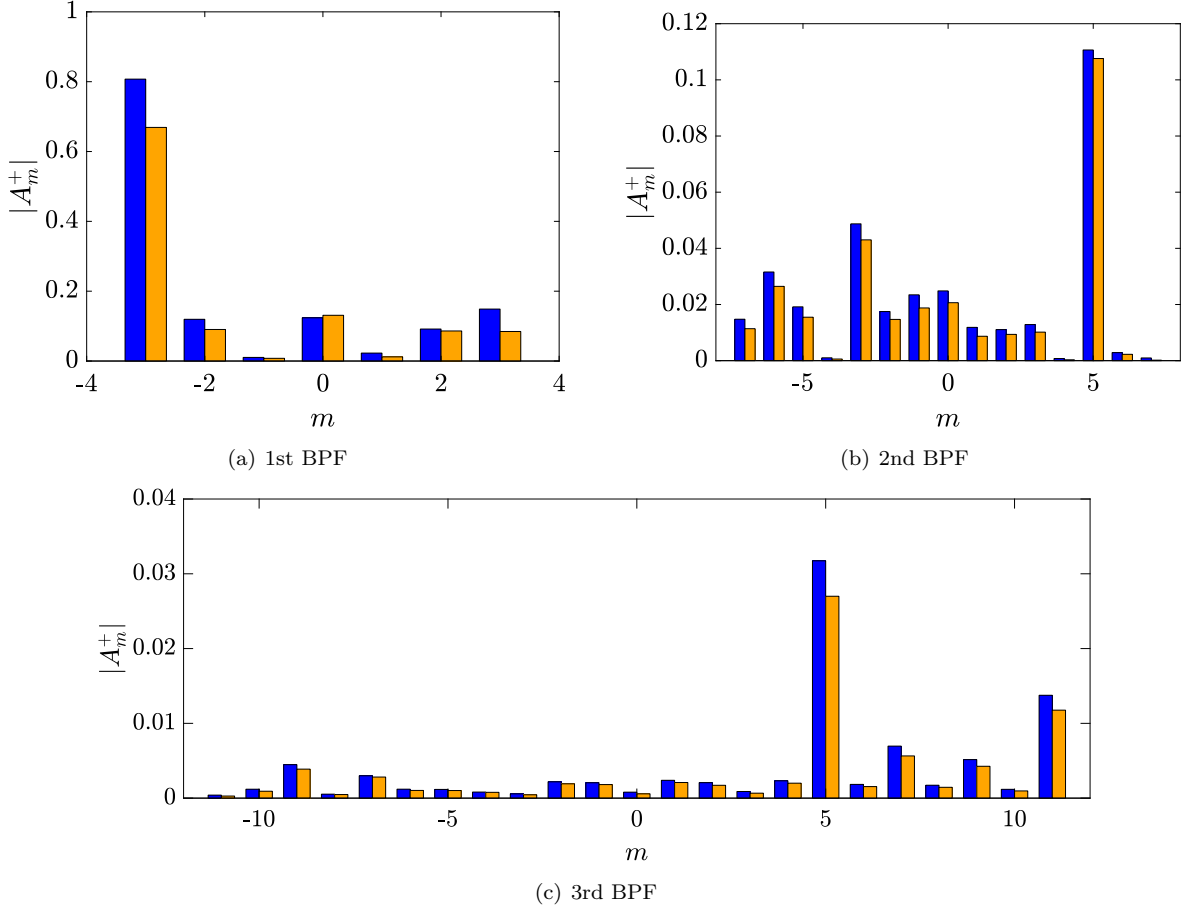


Figure 22. Tonal modal content of the downstream array with TCS. Frequency analysis in blue and engine order analysis in orange. $Q_m = 0.82 \text{ kg}\cdot\text{s}^{-1}$ and $\Delta P = 1980 \text{ Pa}$

parameter (close to 1 in our case) and K_{mn} are the duct eigenvalues.

From the previous wave-number, the axial evolution of several modes can be calculated by the following function:

$$f(x) = e^{ik_{mn}x} \quad (9)$$

It is easily seen that when the wave-number becomes complex, the exponent of the exponential will have a real part corresponding to the damping of the mode. A study has then been carried out for the two rotational speeds. The parameters of the study are summarized in Tab. 3.

Radial order	$n = 0$
Azimuthal order	$m \in [1, 5]$
Rotational speed [rpm]	$\Omega = 9000 \text{ et } 10000$

Table 3. Cut-off modes study parameters

The axial evolution of the modes is plotted in Fig. 23 for the two rotational speeds. In the 10000 rpm case of, modes $m = [1, 2, 3]$ are seen to be cut-on and the first cut-off mode $m = 4$ decays rapidly not interfering on both arrays. However, for a 9000 rpm rotational speed, the decay of the first cut-off mode $m = 3$ is relatively small, which cannot be measured by the microphones of the upstream antenna. This weak rate of decrease is explained by the fact that the frequency of interest (1BPF at 9000rpm) is very close to the cut-off frequency.

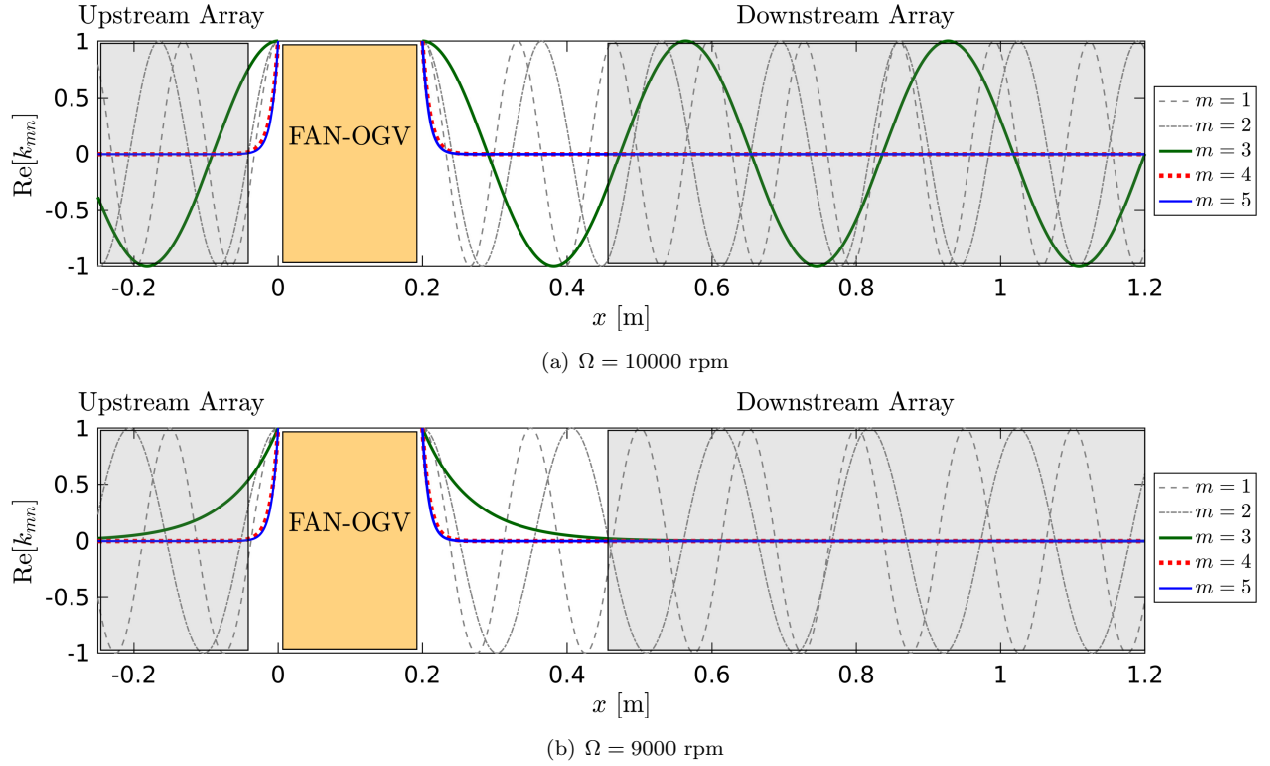


Figure 23. Axial evolution of the first 5 azimuthal modes computed from the function $f(x)$ (Eq. 8) at the first BPF for two rotational speeds.

This study shows the need to account for some cut-off modes to ensure a relevant modal decomposition at 9000 rpm for the upstream array. Indeed, some modes have been added to the modal basis and their decay rate calculated from Eq. 8. The result for the first BPF is shown in Fig. 24. On this calculation two cut-off modes were taken into account in the modal basis: the modes $m = -3$ and $m = 3$. After calculation, it is observed that the mode $m = -3$ has a greater amplitude than the cut-on modes. This is consistent with the results for the 10000 rpm rotational speed (shown in Fig. 24(a)) where the mode $m = -3$ is seen to be dominant at the first BPF.

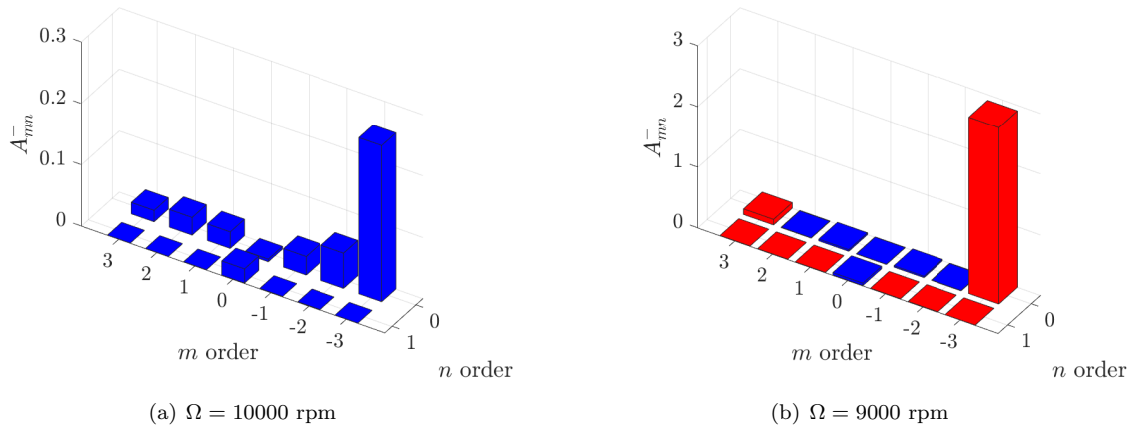


Figure 24. Modal decomposition at the first BPF for $\Omega = 9000$ rpm and 10000 rpm. Cut-off modes in red and cut-on in blue

Nevertheless, it should be noted that the calculation of the amplitude of the cut-off mode is very dependent

on the choice of the source generation plane. For this study, the chosen position was the rotor leading edge but no evidence exists that the mode was actually generated at this position. A possible way of improvement of the method would consist in performing an optimization of the source position to maximize the fit between the reconstructed pressure and the measured pressure. This should allow one to obtain an equivalent source plane that maximizes the quality of the modal decomposition.

Finally, if rotor-stator interaction modes are considered to be independent of the rotational shaft speed, the mode $m = -3$ generated at 9000 rpm and 10000 rpm could be attributed to the stator row heterogeneity.

V. Concluding remarks

An experimental and numerical investigation of a low-speed ducted axial fan was carried out. The numerical and experimental results are in good agreement regarding the pressure ratio / mass flow rate characteristics. A drop of the pressure ratio attributed to the rotating stall is observed after reaching the minimum mass flow rate. The numerical simulation allowed a qualitative evaluation and the assessment of this rotating stall phenomenon. An increasing flow detachment appears for higher pressure rises on the rotor blades when approaching the stall conditions.

The investigation of hot-wire measurements in the inlet assessed the turbulence control screen effectiveness regarding the flow homogenization.

In terms of acoustics, the first two blade passing frequencies (which should be cut-off by the duct for an equivalent homogeneous stator row) were observed to be highly contributing to the acoustic spectrum upstream and downstream of the fan. The removal of the inlet flow distortion by means of the turbulence control screen removed the BPF scattering but did not cancel them.

Modal decompositions for the whole spectra were also performed. The broadband modal content is in agreement with previous results with the energy being fairly concentrated near the cut-off boundary. Regarding the tonal noise, modal decompositions based on time and rotor-locked averaged signals have been compared. The same modal content has been identified with both approaches. The rotational shaft speed variations were then shown to have a negligible impact. The stator heterogeneity is expected to be at the origin of the modal content measured at the first two BPFs.

Finally, the study of a different rotational speed has shown the necessity of taking into account some cut-off modes in the modal basis if the microphone array is placed close to the fan module. At the first blade passing frequency, results have shown the presence of a common dominant mode, cut-off at 9000 rpm but cut-on at 10000 rpm. It is known that the azimuthal orders of modes generated by the rotor-stator interaction are independent of the operating point. Thus, common modes identified at different rotational speeds are expected to be caused by the stator heterogeneity.

Future numerical simulations on a full angular domain comparing both homogeneous and heterogeneous stator configurations will be performed. Finally, a new OGV grid with 23 identical stator vanes is currently under design, and should be subsequently tested to confirm the heterogeneous impact of the OGV grid on the noise radiation investigated in this paper.

Acknowledgments

This research has been funded by Safran Aircraft Engines and by the French National Research Agency (ANR) through the ADOPSYS industrial chair, and also by the Labex CeLyA of Université de Lyon, operated by the French National Research Agency (ANR-10-LABX-0060/ ANR-11-IDEX-0007). The authors acknowledge Patrice Caule from Technofan for providing the *LP3* fan-OGV module. The authors would also like to thank Jean-Michel Perrin for all the help in setting up the experiment.

A. Appendix: duct modal basis parameters

Parameters of the duct modal basis are given in this appendix. Radial shape functions for a cylindrical duct are defined as

$$f_{mn}(r) = J_m(K_{mn}r) \quad (10)$$

where K_{mn} are the duct eigenvalues. The radial shape normalization factors are given by

$$\Gamma_{mn} = \int_{R_{\text{hub}}}^{R_{\text{tip}}} f_{mn}(r)^2 r dr = \pi \left[r^2 f_{mn}^2(r) \left(1 - \frac{m^2}{K_{mn}^2 r^2} \right) \right]_{R_{\text{hub}}}^{R_{\text{tip}}} \quad (11)$$

The wave-number γ_{mn}^{\pm} is defined as

$$\gamma_{mn}^{\pm} = \frac{M_0 k_0}{\beta^2} \pm \frac{k_{mn}}{\beta^2} \quad (12)$$

with $\beta = \sqrt{1 - M_0^2}$, $k_0 = \omega/U_0$ and the axial wave-number given by

$$k_{mn} = \sqrt{k_0^2 - \beta^2 K_{mn}^2} \quad (13)$$

References

- ¹Sanjose, M., Pestana, M., Moreau, S., and Roger, M., "Influence and modeling of OGV heterogeneity," 22nd AIAA/CEAS Aeroacoustics Conference, 2016, p. 2881.
- ²Bonneau, V., Polacsek, C., Barrier, R., Lewy, S., Roux, J.-M., and Gervais, Y., "Tonal Noise Prediction of a Turbofan with Heterogeneous Stator and Bifurcations," AIAA Journal, Vol. 53, No. 11, 2015, pp. 3354–3369.
- ³Roger, M. and Caule, P., "Assesment of the Effect of Stator Inhomogeneity on Rotor-Stator Tonal Noise," ISROMAC-15, 2014.
- ⁴Pereira, A., Finez, A., Leclere, Q., Salze, E., and Souchotte, P., "Modal identification of a small-scale ducted fan," 22nd AIAA/CEAS Aeroacoustics Conference, 2016, p. 3063.
- ⁵Tyler, J. M. and Sofrin, T. G., "Axial flow compressor noise studies," Tech. rep., SAE Technical Paper, 1962.
- ⁶Finez, A., Pereira, A., and Leclere, Q., "Broadband mode decomposition of ducted fan noise using cross-spectral matrix denoising," Fan Noise 2015, 2015.
- ⁷Salze, É., Bailly, C., Marsden, O., Jondeau, E., and Juvé, D., "An experimental characterisation of wall pressure wavevector-frequency spectra in the presence of pressure gradients," 20th AIAA/CEAS Aeroacoustics Conference, 2014, p. 2909.
- ⁸Leclère, Q., Pereira, A., Finez, A., and Souchotte, P., "Indirect calibration of a large microphone array for in-duct acoustic measurements," Journal of Sound and Vibration, Vol. 376, 2016, pp. 48–59.
- ⁹Menter, F., Kuntz, M., and Langtry, R., "Ten years of industrial experience with the SST turbulence model," Turbulence, heat and mass transfer, Vol. 4, No. 1, 2003, pp. 625–632.
- ¹⁰Lakshminarayana, B., "Fluid Dynamics and Heat Transfer of Turbomachinery," 1996.
- ¹¹Sturm, M. and Carolus, T., "Large scale inflow distortions as a source mechanism for discrete frequency sound from isolated axial fans," 19th AIAA/CEAS Aeroacoustics Conference, 2013, p. 2105.
- ¹²Sturm, M., Sanjosé, M., Moreau, S., and Carolus, T., "Aeroacoustic simulation of an axial fan including the full test rig by using the Lattice Boltzmann Method," 2015.
- ¹³Zambonini, G. and Ottavy, X., "Unsteady pressure investigations of corner separated flow in a linear compressor cascade," ASME Turbo Expo 2015: Turbine Technical Conference and Exposition, American Society of Mechanical Engineers, 2015, pp. V02CT44A002–V02CT44A002.
- ¹⁴Sturm, M., Sanjosé, M., Moreau, S., and Carolus, T., "Aeroacoustics simulation of an axial fan including the full test rig by using the Lattice Boltzmann Method," 2015.
- ¹⁵Farassat, F., Nark, D. M., and Thomas, R. H., "The Detection of Radiated Modes From Ducted Fan Engines," 7th AIAA/CEAS Aeroacoustics Conference, Maastricht, The Netherlands, 2001, No. 2138, 2001.
- ¹⁶Rademaker, E., Sijtsma, P., and Tester, B., "Mode detection with an optimised array in a model turbofan engine intake at varying shaft speeds," 7th AIAA/CEAS Aeroacoustics Conference and Exhibit, 2001, p. 2181.
- ¹⁷Enghardt, L., Neuhaus, L., and Lowis, C., "Broadband sound power determination in flow ducts," 10th AIAA/CEAS Aeroacoustics Conference, American Institute of Aeronautics and Astronautics, 2004, AIAA 2004-2940.
- ¹⁸Lewy, S., "Inverse method predicting spinning modes radiated by a ducted fan from free-field measurements," The Journal of the Acoustical Society of America, Vol. 117, No. 2, 2005, pp. 744–750.

- ¹⁹Castres, F. O. and Joseph, P. F., “Experimental investigation of an inversion technique for the determination of broadband duct mode amplitudes by the use of near-field sensor arrays,” The Journal of the Acoustical Society of America, Vol. 122, No. 2, 2007, pp. 848–859.
- ²⁰Castres, F. O. and Joseph, P. F., “Mode detection in turbofan inlets from near field sensor arrays,” The Journal of the Acoustical Society of America, Vol. 121, No. 2, 2007, pp. 796–807.
- ²¹Bennett, G. J., O’Reilly, C., Tapken, U., and Fitzpatrick, J., “Noise source location in turbomachinery using coherence based modal decomposition,” Proceedings of the 15th AIAA/CEAS Aeroacoustics Conference, Miami, FL, USA, No. 3367, 2009.
- ²²Tapken, U., Raitor, T., and Enghardt, L., “Tonal Noise Radiation From an UHBR Fan - Optimized In-Duct Radial Mode Analysis,” Proceedings of the 15th AIAA/CEAS Aeroacoustics Conference, Miami, FL, USA, No. 3288, 2009.
- ²³Munjal, M., Acoustics of Ducts and Mufflers With Application to Exhaust and Ventilation System Design, Wiley-Interscience publication, Wiley, 1987.
- ²⁴Rienstra, S. and Hirschberg, A., “An introduction to acoustics,” Report IWDE, 2001.
- ²⁵Chung, J. Y., “Rejection of flow noise using a coherence function method,” The Journal of the Acoustical Society of America, Vol. 62, No. 2, 1977, pp. 388–395.
- ²⁶Bultè, J., “Acoustic Array Measurements in Aerodynamic Wind Tunnels: A Subspace Approach for Noise Suppression,” 13th AIAA/CEAS Aeroacoustics Conference, Rome, Italy, 2007.
- ²⁷Druault, P., Hekmati, A., and Ricot, D., “Discrimination of acoustic and turbulent components from aeroacoustic wall pressure field,” Journal of Sound and Vibration, Vol. 332, No. 26, 2013, pp. 7257 – 7278.
- ²⁸Premo, J. and Joppa, P., “Fan noise source diagnostic test-wall measured circumferential array mode results,” 8th AIAA/CEAS Aeroacoustics Conference & Exhibit, 2002, p. 2429.
- ²⁹Ganz, U. W., Joppa, P. D., Patten, T. J., and Scharpf, D. F., “Boeing 18-inch fan rig broadband noise test,” 1998.